

Parametric amplification of Rydberg six- and eight-wave mixing processes

ZHAOYANG ZHANG,[†] JI GUO,[†] BINGLING GU, LING HAO, GAOGUO YANG, KUN WANG,
AND YANPENG ZHANG*

Key Laboratory for Physical Electronics and Devices of the Ministry of Education & Shaanxi Key Laboratory of Information Photonic Technique, Xi'an Jiaotong University, Xi'an 710049, China

*Corresponding author: ypzhang@mail.xjtu.edu.cn

Received 26 February 2018; revised 26 April 2018; accepted 26 April 2018; posted 27 April 2018 (Doc. ID 324899); published 18 June 2018

We study the parametric amplification of electromagnetically induced transparency-assisted Rydberg six- and eight-wave mixing signals through a cascaded nonlinear optical process in a hot rubidium atomic ensemble both theoretically and experimentally. The shift of the resonant frequency (induced by the Rydberg–Rydberg interaction) of parametrically amplified six-wave mixing signal is observed. Moreover, the interplays between the dressing effects and Rydberg–Rydberg interactions in parametrically amplified multiwave mixing signals are investigated. The linear amplification of Rydberg multiwave mixing processes with multichannel nature acts against the suppression caused by Rydberg–Rydberg interaction and dressing effect. © 2018 Chinese Laser Press

OCIS codes: (020.5780) Rydberg states; (190.4223) Nonlinear wave mixing; (190.4380) Nonlinear optics, four-wave mixing; (190.4410) Nonlinear optics, parametric processes.

<https://doi.org/10.1364/PRJ.6.000713>

1. INTRODUCTION

Atoms excited to Rydberg states have attracted considerable interest owing to their excellent properties, such as long lifetimes, large collision cross sections, large dipole moments, and gigantic spatial extension [1]. Besides, Rydberg–Rydberg interaction (RRI) between Rydberg atoms, such as dipole–dipole interaction and van der Waals interaction, can induce the dipole blockade of nearby atoms [2,3]. These properties lead to a large amount of prospective applications, such as quantum information processing [4,5], high-fidelity optical state control [6], and single-photon sources [7]. For these applications, detecting Rydberg dressing-state effect and the interactions among the Rydberg atoms nondestructively is a basic requirement. Recently, electromagnetically induced transparency (EIT) [8–12] and multiwave mixing (MWM) [13–15] as nondestructive optical detection methods [16,17] have been proposed and utilized for detecting Rydberg atoms [18,19] where the Rydberg atoms are not ionized. The multichannel nature of the MWM process allows for multichannel information processing related to Rydberg states. Furthermore, the MWM process can act as a multimode correlated light source [20]. However, MWM signals generated from high-order nonlinear optical processes such as six-wave mixing (SWM) and eight-wave mixing (EWM) are much weaker than EIT signals [21]. In addition, Rydberg excitation can further suppress the signal intensity and decrease the signal-to-noise ratio [22].

The optical parametric amplification (OPA) process, which can act as an optical amplifier and implement the linear amplification of the input signal [23], is proposed and experimentally achieved in the media of both gaseous and solid states [24,25]. Generally, the OPA process in an atomic medium is characterized by the so-called conical emission [26], where two correlated photons named as Stokes and anti-Stokes photons are effectively generated [27]. The OPA process can be achieved by the cascaded nonlinear process, in which the generated MWM signals coexist with the parametrical FWM process [20,28]. Intensity noise correlation [29] and intensity-difference squeezing [30] of such a process have given rise to applications in quantum metrology [31–33]. Inspired by such an OPA process, the high-order Rydberg MWM signal can also be injected into the Stokes or anti-Stokes port and then be linearly and nondestructively amplified to enhance the signal-to-noise ratio of the Rydberg MWM signal. As a result, the performance of applications related to Rydberg excitations such as sensors [31–35] can be promisingly improved via OPA.

In this paper, we observed the Rydberg parametrically amplified MWM (PA-MWM) signals assisted by the cascaded nonlinear process in a *K*-type five-level system of ⁸⁵Rb. With two EIT windows generated effectively, the parametrically amplified SWM (PA-SWM) and EWM (PA-EWM) signals can be simultaneously detected. Meanwhile, the intensities of PA-MWM signals can be controlled by the detuning and the

power of the coupling fields as well as the density of the atomic ensemble. Moreover, the saturation of the signal intensity and the shift of the resonant position caused by the RRI when changing the beam power and temperature can be detected. Finally, the suppression (enhancement) of coexisting PA-SWM and PA-EWM signals near resonance (far from resonance) is observed. These phenomena in the Rydberg PA-MWM process can improve the applications related to Rydberg atoms in the fields of quantum metrology and sensors.

2. BASIC THEORY AND EXPERIMENTAL SETUP

In the K -type five-level ^{85}Rb atomic system shown in Fig. 1(a), two hyperfine energy levels, $F = 3$ ($|0\rangle$) and $F = 2$ ($|3\rangle$), of the ground state $5S_{1/2}$, a Rydberg excited state $nD_{5/2}$ ($|2\rangle$), and two lower excited states, $5P_{3/2}$ ($|1\rangle$) and $5D_{5/2}$ ($|4\rangle$), are connected by corresponding beams. The experimental configuration is shown in Fig. 1(b). Five beams derived from four external cavity diode lasers (ECDLs) with linewidths < 1 MHz are used to couple the following transitions. The transition $|0\rangle \leftrightarrow |1\rangle$ is probed by beam E_1 [wavelength of 780.2 nm, frequency ω_1 , wave vector \mathbf{k}_1 , and Rabi frequency G_1 , defined as $G_i = \mu_{ij}E_i/\hbar$, where μ_{ij} is the dipole moment between $|i\rangle \leftrightarrow |j\rangle$ ($i, j = 1, 2, 3, 4$)]. The Rydberg transition $|1\rangle \leftrightarrow |2\rangle$ is connected by a strong beam E_2 (~ 480 nm, ω_2 , \mathbf{k}_2 , G_2), which propagates opposite to beam E_1 . The transition $|1\rangle \leftrightarrow |3\rangle$ is connected by two beams E_3 (780.2 nm, ω_3 , \mathbf{k}_3 , G_3) and E'_3 (780.2 nm, ω'_3 , \mathbf{k}'_3 , G'_3), which are derived from the same ECDL. In the atomic ensemble, E_3 propagates in the same direction with E_2 , while E'_3 has a small angle of 0.3° with E_3 . The transition $|1\rangle \leftrightarrow |4\rangle$ is driven by the beam E_4 (775.9 nm, ω_4 , \mathbf{k}_4 , G_4), whose propagation is symmetrical to E'_3 about E_2 .

A. Rydberg MWM Process

By turning these lasers on and off selectively, we can get different MWM signals with different orders. When the beams E_2 and E_4 are blocked, an FWM process satisfying the phase-matching condition $\mathbf{k}_{\text{FWM}} = \mathbf{k}_1 + \mathbf{k}_3 - \mathbf{k}'_3$ will occur in the

three-level subsystem $|0\rangle \leftrightarrow |1\rangle \leftrightarrow |3\rangle$. When only the beam E_2 with Rydberg dressing-state effect is blocked, an SWM process (denoted as SWM1) satisfying the phase-matching condition $\mathbf{k}_{\text{SWM1}} = \mathbf{k}_1 + \mathbf{k}_3 - \mathbf{k}'_3 + \mathbf{k}_4 - \mathbf{k}_4$ will occur in a four-level subsystem $|0\rangle \leftrightarrow |1\rangle \leftrightarrow |3\rangle \leftrightarrow |4\rangle$, in which one photon each from E_1 , E_3 , E'_3 , and two photons from E_4 are involved. Similarly, by blocking E_4 , another SWM process (denoted as SWM2) with $\mathbf{k}_{\text{SWM2}} = \mathbf{k}_1 + \mathbf{k}_3 - \mathbf{k}'_3 + \mathbf{k}_2 - \mathbf{k}_2$ can be observed in the subsystem $|0\rangle \leftrightarrow |1\rangle \leftrightarrow |2\rangle \leftrightarrow |3\rangle$. When all the beams shown in Fig. 1(b) are on, a new EWM signal can be generated with phase-matching condition $\mathbf{k}_{\text{EWM}} = \mathbf{k}_1 + \mathbf{k}_2 - \mathbf{k}_2 + \mathbf{k}_3 - \mathbf{k}'_3 + \mathbf{k}_4 - \mathbf{k}_4$ in the five-level atomic system $|0\rangle \leftrightarrow |1\rangle \leftrightarrow |2\rangle \leftrightarrow |3\rangle \leftrightarrow |4\rangle$. It can be revealed from the phase-matching conditions that these MWM signals emit in the direction opposite to E'_3 . These signals are detected by the avalanche photodiode detectors (APDs). To be specific, the EIT signal is received by D1, and the MWM signals are received by D2, as shown in Fig. 1(b).

Generally, the response of the atoms to the light is described by the susceptibility. The generated MWM signals are characterized by their nonlinear susceptibilities $\chi^{(2n+1)} = \rho_{00}\mu_{10}\rho_{10}^{(2n+1)}/\epsilon_0 E_1$ (e.g., $n = 1$ for FWM, $n = 2$ for SWM, and $n = 3$ for EWM). According to the perturbation chain $\rho_{00}^{(0)} \xrightarrow{E_1} \rho_{10}^{(1)} \xrightarrow{E_3} \rho_{30}^{(2)} \xrightarrow{(E'_3)^*} \rho_{10}^{(3)}$ via the Liouville pathway [36], the density-matrix element for the E_{FWM} is given by

$$\rho_{10}^{(3)} = \frac{iG_1|G_3|^2 e^{ik_{\text{FWM}} \cdot r}}{(d'_1 + |G_1|^2/\Gamma_{00})^2 d'_3}, \quad (1)$$

where $d'_1 = \Gamma_{10} + i(\Delta_1 + k_1 v)$ and $d'_3 = \Gamma_{30} + i(\Delta_1 - \Delta_3) + i(k_1 v + k_3 v)$, Γ_{ij} is the decay rate between states $|i\rangle$ and $|j\rangle$, and $\Delta_i = \Omega_{ij} - \omega_i$ is the detuning between the frequency ω_i of beam E_i and the resonant transition frequency Ω_{ij} between $|i\rangle \leftrightarrow |j\rangle$; $k_i v$ is the term of the Doppler effect.

Considering the upper transition $|1\rangle \leftrightarrow |4\rangle$, the SWM1 signal is generated with the help of the EIT windows ($\Delta_1 + \Delta_4 = 0$). The perturbation chain for this process can be written as $\rho_{00}^{(0)} \xrightarrow{E_1} \rho_{10}^{(1)} \xrightarrow{E_3} \rho_{30}^{(2)} \xrightarrow{(E'_3)^*} \rho_{10}^{(3)} \xrightarrow{E_4} \rho_{40}^{(4)} \xrightarrow{E_4^*} \rho_{10}^{(5)}$.

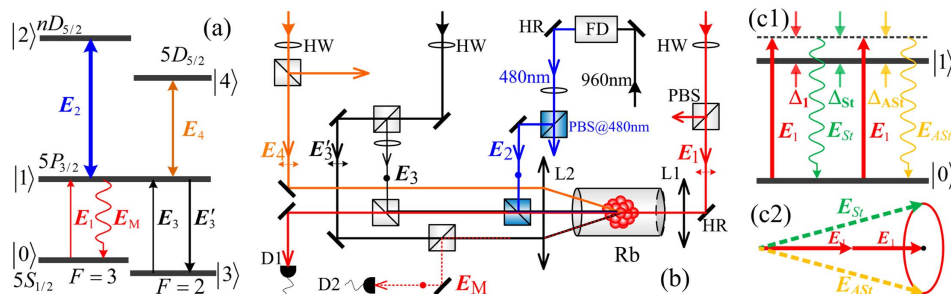


Fig. 1. (a) Five-level K -type energy level diagram depicting the generation of the MWM process in the ^{85}Rb atomic system. (b) Experimental setup. D, photodetector; L, lens; PBS, polarized beam splitter at corresponding wavelength; FD, frequency doubler; HR, high-reflectivity mirror; HW, half-wave plate at corresponding wavelength. Transverse double-headed arrows and filled dots indicate the horizontal polarization and vertical polarization of incident beams, respectively. Five beams derived from the four laser systems are coupled into the 10 mm long Rb cell wrapped with μ -metal sheets. The transition $|0\rangle \leftrightarrow |1\rangle$ is coupled by the beam E_1 (780.2 nm). Rydberg transition $|1\rangle \leftrightarrow |2\rangle$ is coupled by beam E_2 (480 nm), which counterpropagates with beam E_1 . $|1\rangle \leftrightarrow |3\rangle$ is connected by beams E_3 and E'_3 (780.2 nm), which are derived from the same ECDL, and $|1\rangle \leftrightarrow |4\rangle$ is coupled by beam E_4 (775.9 nm). The EIT signal and MWM spectrum signals are received by D1 and D2, respectively. (c1) Energy schematic diagram for SP-FWM process; (c2) phase-matching condition of SP-FWM process.

Considering the strong field dressing effect of \mathbf{E}_4 in the dressed perturbation chain [27,37], one can get

$$\rho_{10}^{(5)} = \frac{iG_1|G_3|^2|G_4|^2 e^{ik_{\text{SWM1}} \cdot r}}{(d_1 + |G_1|^2/\Gamma_{00} + |G_4|^2/d_4)^3 d_3 d_4}, \quad (2)$$

where $d_1 = \Gamma_{10} + i\Delta_1$, $d_3 = \Gamma_{30} + i(\Delta_1 - \Delta_3)$ and $d_4 = \Gamma_{40} + i(\Delta_1 + \Delta_4)$.

The SWM2 signal is obtained in the EIT windows ($\Delta_1 + \Delta_2 = 0$), and the EWM is obtained in the two overlapped EIT windows ($\Delta_1 + \Delta_2 = 0$ and $\Delta_1 + \Delta_4 = 0$). The SWM2 and EWM processes are described by the perturbation chains $\rho_{00}^{(0)} \xrightarrow{E_1} \rho_{10}^{(1)} \xrightarrow{E_3} \rho_{30}^{(2)} \xrightarrow{(E_3)^*} \rho_{10}^{(3)} \xrightarrow{E_2} \rho_{20}^{(4)} \xrightarrow{E_2^*} \rho_{10}^{(5)}$ and $\rho_{00}^{(0)} \xrightarrow{E_1} \rho_{10}^{(1)} \xrightarrow{E_3} \rho_{30}^{(2)} \xrightarrow{(E_3)^*} \rho_{10}^{(3)} \xrightarrow{E_2} \rho_{20}^{(4)} \xrightarrow{(E_2)^*} \rho_{10}^{(5)} \xrightarrow{E_4} \rho_{40}^{(6)} \xrightarrow{E_4^*} \rho_{10}^{(7)}$, respectively.

Similarly, we can get the density-matrix elements for \mathbf{E}_{SWM2} and \mathbf{E}_{EWM} related to the Rydberg level $|2\rangle$, while besides the strong field dressing effect of \mathbf{E}_2 in the dressed perturbation chain, the RRI induced by \mathbf{E}_2 should be considered. Atoms excited to the Rydberg energy level ($|2\rangle$) can shift the energy levels of the nearby atoms, and thus significantly suppress the rate of Rydberg transitions from $|1\rangle$ to $|2\rangle$. To make our model adaptive in the case of Rydberg excitation, we can substitute terms ρ_0 , G_1 , G_2 , and G_3 in the classical model with $\rho_0^{0.2}$, $G_1^{0.2}$, $(G_2/n^{11})^{0.2}$, and $G_3^{0.2}$ (see Appendix A). The respective density-matrix elements for \mathbf{E}_{SWM2} and \mathbf{E}_{EWM} can be given by

$$\rho_{10}^{(5)} = \frac{iG_1^{0.2}(|G_2/n^{11}|)^{0.4}|G_3|^{0.4} e^{ik_{\text{SWM2}} \cdot r}}{[d_1 + |G_1|^{0.4}/\Gamma_{00} + (|G_2/n^{11}|)^{0.4}/d_2]^3 d_2 d_3}, \quad (3)$$

and

$$\rho_{10}^{(7)} = \frac{iG_1^{0.2}(|G_2/n^{11}|)^{0.4}|G_3|^{0.4}|G_4|^2 e^{ik_{\text{EWM}} \cdot r}}{\left(d_1 + \frac{|G_1|^{0.4}}{\Gamma_{00}} + \frac{(|G_2/n^{11}|)^{0.4}}{d_2} + \frac{|G_4|^2}{d_4}\right)^4 d_2 d_3 d_4}, \quad (4)$$

where $d_2 = \Gamma_{20} + i(\Delta_1 + \Delta_2)$.

B. OPA Process

Considering the degenerate two-level atomic configuration in Fig. 1(c1) driven by \mathbf{E}_1 , the spontaneous parametric four-wave mixing (SP-FWM) process, which generates two output weak signals (Stokes signal \mathbf{E}_{St} and anti-Stokes signal \mathbf{E}_{ASt}), will occur in the subsystem $|0\rangle \leftrightarrow |1\rangle$ [20,28], known as the conical emission [26]. The signals in the Stokes port and the anti-Stokes port satisfy the phase-matching condition $\mathbf{k}_{\text{St}} = 2\mathbf{k}_1 - \mathbf{k}_{\text{ASt}}$ and $\mathbf{k}_{\text{ASt}} = 2\mathbf{k}_1 - \mathbf{k}_{\text{St}}$, respectively, which are shown in Fig. 1(c2).

According to the perturbation chains $\rho_{00}^{(0)} \xrightarrow{E_1} \rho_{10}^{(1)} \xrightarrow{E_{\text{ASt}}} \rho_{10(\text{St})}^{(2)} \xrightarrow{E_1} \rho_{10(\text{St})}^{(3)}$ and $\rho_{00}^{(0)} \xrightarrow{E_1} \rho_{10}^{(1)} \xrightarrow{E_{\text{St}}} \rho_{10(\text{ASt})}^{(2)} \xrightarrow{E_1} \rho_{10(\text{ASt})}^{(3)}$ of the Stokes and anti-Stokes channels, their respective density-matrix elements can be given as

$$\rho_{20(\text{St})}^{(3)} = \frac{-i|G_1|^2 G_{\text{ASt}}^*}{d_1 d'_{00} d'_{10}}, \quad (5)$$

and

$$\rho_{20(\text{ASt})}^{(3)} = \frac{-i|G_1|^2 G_{\text{St}}^*}{d_1 d'_{00} d'_{10}}, \quad (6)$$

where $d'_{00} = \Gamma_{00} + i(\Delta_1 - \Delta_{\text{ASt}})$, $d'_{10} = \Gamma_{10} + i(2\Delta_1 - \Delta_{\text{St}})$, $d''_{00} = \Gamma_{00} + i(\Delta_1 - \Delta_{\text{St}})$, and $d''_{10} = \Gamma_{10} + i(2\Delta_1 - \Delta_{\text{ASt}})$.

When the generated MWM waves propagate along with the Stokes beam and have the same frequency as the Stokes signal, it is considered that the MWM signals are injected into the Stokes port and then parametric amplification is achieved [23]. Such amplified signals are termed as PA-MWM signals. The photon numbers of the output Stokes and anti-Stokes fields of the OPA process are [38]

$$\langle \hat{a}_{\text{out}}^+ \hat{a}_{\text{out}} \rangle = g \langle \hat{a}_{\text{in}}^+ \hat{a}_{\text{in}} \rangle + (g - 1), \quad (7)$$

and

$$\langle \hat{b}_{\text{out}}^+ \hat{b}_{\text{out}} \rangle = (g - 1) \langle \hat{a}_{\text{in}}^+ \hat{a}_{\text{in}} \rangle + (g - 1), \quad (8)$$

where $\hat{a}(\hat{a}^+)$ and $\hat{b}(\hat{b}^+)$ are the annihilation (creation) operator of \mathbf{E}_{St} and \mathbf{E}_{ASt} , and $g = \{\cos[2t\sqrt{AB} \sin(\varphi_1 + \varphi_2)/2] + \cosh[2t\sqrt{AB} \cos(\varphi_1 + \varphi_2)/2]\}/2$ is the gain of the process with the modules A and B (phases φ_1 and φ_2) defined in $\rho_{10(\text{St})}^{(3)} = A e^{i\varphi_1}$ and $\rho_{10(\text{ASt})}^{(3)} = B e^{i\varphi_2}$ for \mathbf{E}_{St} and \mathbf{E}_{ASt} , respectively. From Eqs. (7) and (8), the output signal is amplified by the factor g in the Stokes port and $g - 1$ in the anti-Stokes port.

3. EXPERIMENTAL RESULTS

At first, with all of the beams on except \mathbf{E}_4 , as is shown in Fig. 2(a1), the SWM2 signal (generated in the inverted-Y-type four-level subsystem $|0\rangle \leftrightarrow |1\rangle \leftrightarrow |2\rangle \leftrightarrow |3\rangle$) with the effect of RRI as well as an FWM signal (serving as the background) is injected into the Stokes port of the SP-FWM [in Figs. 2(a2) and 2(a3)] process. Then, the generated PA-SWM2 signal is detected by the APD. Such signal is observed by scanning Δ_1 at different values of Δ_2 . The dashed lines in Figs. 2(b1) and 2(b2) represent the background PA-FWM signal, upon which the prominent peaks indicate PA-SWM2 signals. In Figs. 2(c1) and 2(c2), the SWM signals related to the fine structure of energy level ($37D_{3/2}$ and $54D_{3/2}$) of the Rb atoms are revealed. In this case, the intensities of these PA-SWM2 signals are weaker, because the dipole moment μ_{ij} between $5P_{3/2}$ and $nD_{5/2}$ is larger than that between $5P_{3/2}$ and $nD_{3/2}$. For PA-SWM2 signals whose generation is related to $nD_{3/2}$, the fluctuation of the background PA-FWM signal plays a significant role with respect to the pure PA-SWM2 signal, as shown in Figs. 2(c1) and 2(c2). The intensity of the PA-SWM2 signal transited from $nD_{5/2}$ is much stronger than that transited from $nD_{3/2}$. Hence, the fluctuations of the same background PA-FWM signals are much weaker in contrast to pure PA-SWM2 signals, which can be seen in Figs. 2(b1) and 2(b2). Therefore, the PA-SWM2 signals transited from $nD_{5/2}$ have a higher signal-to-noise ratio than that transited from $nD_{3/2}$.

In Figs. 2(d1) and 2(d2), we investigate the effect of RRI by comparing the detuning of the dressing field in the PA-SWM2 process with that in the non-Rydberg PA-SWM1 process. With the non-Rydberg dressing field \mathbf{E}_4 turned on and Rydberg dressing field \mathbf{E}_2 turned off, the PA-SWM1 signal is obtained

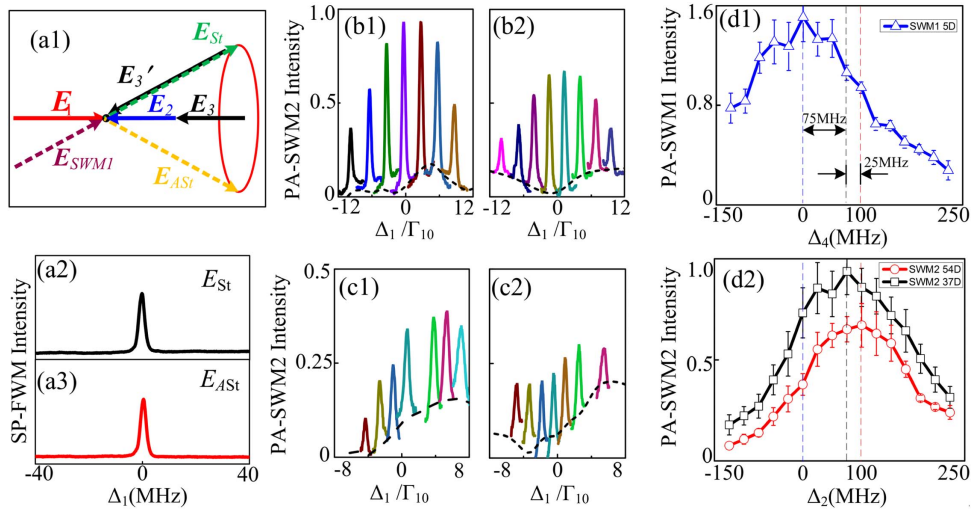


Fig. 2. (a1) Phase-matching diagram of the OPA process with E_{SWM1} injected into the Stokes port. (a2) Measured Stokes field E_{St} and (a3) anti-Stokes field E_{ASt} versus Δ_1 ; (b1) and (b2) intensity of PA-SWM2 signals transited from $nD_{5/2}$ versus Δ_1 at different Δ_2 for $n = 37$ and $n = 54$, respectively; (c1) and (c2) intensity of PA-SWM2 signals transited from fine structure of energy level $nD_{3/2}$ versus Δ_1 at different Δ_2 for $n = 37$ and $n = 54$, respectively; (d1) PA-SWM1 signals (denoted as blue triangles) versus Δ_1 at different Δ_4 ($\Delta_1 + \Delta_4 = 0$); (d2) PA-SWM2 signals transited from $37D_{5/2}$ (denoted as black squares) and $54D_{3/2}$ (denoted as red circles) versus Δ_1 at different Δ_2 ($\Delta_1 + \Delta_2 + \varepsilon = 0$).

by scanning Δ_1 at the discrete value of Δ_4 . To illustrate that the PA-SWM2 signals are affected by the RRI, here we mainly focus on the value of Δ_1 , where the strongest PA-SWM1 or PA-SWM2 signal is detected for each detuning of the dressing field. From Eq. (2), when Δ_4 is tuned to different values, the PA-SWM1 signals can reach the maximum values at the resonant condition of $\Delta_4 + \Delta_1 = 0$. And when $\Delta_4 + \Delta_1 = 0$ is fulfilled, we can also find that the strongest signal appears at $\Delta_1 = 0$, which indicates $\Delta_4 = 0$. However, the resonant condition of PA-SWM2 should be rewritten as $\Delta_2 + \Delta_1 + \varepsilon = 0$ by taking the energy shift ε caused by the RRI into consideration. In this case, the strongest signal is still observed at the condition of $\Delta_1 = 0$, while at this time Δ_2 is given as $\Delta_2 = -\varepsilon$. The deviation between Δ_2 and Δ_4 can be found in Figs. 2(d1) and 2(d2), which are obtained by considering the conditions of $\Delta_1 + \Delta_2 + \varepsilon = 0$ (for PA-SWM2 signals) and $\Delta_1 + \Delta_4 = 0$ (for PA-SWM1 signals). Here, $\Delta_2 = 0$ is determined at the condition of low-beam power and temperature, where the RRI can be ignored. Compared with the detuning

Δ_4 , which is exactly at the zero point (marked as the blue vertical dashed line), detuning Δ_2 of two PA-SWM2 processes ($n = 37$ and $n = 54$) when the maximum signal intensities are obtained (marked by the black and red vertical dashed lines, respectively) are far from the zero point. We can find that the deviation of Δ_2 between PA-SWM1 and PA-SWM2 signals at the maximum value point also varies with the principal quantum number n of the Rydberg energy level. Comparing the deviation gap of Δ_2 at the condition of $n = 37$ with the gap at $n = 54$, it can be found that the deviation changes from approximately 75 to 100 MHz. This phenomenon indicates that the energy shift ε becomes larger for a higher Rydberg energy level. According to the Appendix A, the energy shift is estimated to be 50 and 115 MHz for $n = 37$ and $n = 54$, respectively, which matches with our experimental result.

In Fig. 3, we show the intensity of Rydberg PA-SWM2 signals subjected to changes in field power and temperature. We obtain the intensity of the PA-SWM2 signals at different

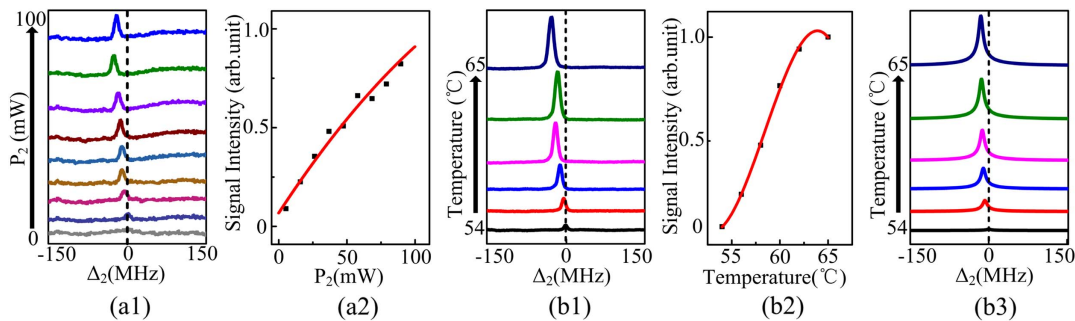


Fig. 3. (a1) Measured PA-SWM2 signals versus Δ_2 by increasing P_2 for $n = 37$; (a2) intensity dependence of the PA-SWM2 signals corresponding to (a1) on P_2 ; (b1) measured PA-SWM2 signals versus Δ_2 by changing the temperature for $n = 37$; (b2) intensity dependence of the PA-SWM2 signals corresponding to (b1) on resonant condition on temperature; (b3) theoretically simulated PA-SWM2 signals to (b1). The dots indicate the experimental data, and the solid curve represents the theoretical simulation. The dashed lines are a guide for the eyes.

power of E_2 by scanning Δ_2 as shown in Fig. 3(a1). Apparently, the intensity of SWM2 signal increases with the power P_2 of E_2 . Besides the demonstrated effects of principal quantum number n [16] and atomic density ρ_0 [39], one can also find that energy shift ε varies slightly with the power of the Rydberg dressing field E_2 (which is related to the Rydberg atomic density given in the Appendix A). To illustrate the effect of changing the field intensity, we replace the term d_2 in the Rydberg-modified fifth-order density-matrix element with $d'_2 = \Gamma_{20} + i(\Delta_1 + \Delta_2 + \varepsilon)$. Then one can predict that laser power P_2 can exert impact on the intensity of the PA-SWM2 signal from two terms, namely, Rabi frequency G_2 and energy shift ε . In particular, G_2 mainly determines the signal intensity, while ε affects not only the signal intensity but also the resonant position. According to Eq. (3) and d'_2 , the maximum intensity of the SWM2 signal is found when the resonant condition ($\Delta_2 = -\Delta_1 - \varepsilon$) is satisfied. As shown in Fig. 3(a1), by scanning the detuning of Rydberg dressing field E_2 , we can find that the value of Δ_2 at the resonant position moves gradually away from zero with the increase of P_2 . This shift of detuning Δ_2 at the resonant point caused by changing the power can be explained quantitatively. The shifting rate of Δ_2 on the power of E_2 can be represented by the first-order derivative of ε with respect to P_2 . Such a derivative can be given as

$$\frac{d\varepsilon}{dP_2} = \frac{2C\mu_{12}^2\rho_0^{0.2}G_2^{-1.6}}{5\varepsilon_0cA\hbar^2n^{0.44}} \left(\frac{G_1^2}{\Gamma_{10} + G_2^2/\Gamma_{20}} + \frac{G_3^2}{\Gamma_{30}} \right)^{-0.8} \times \left(\frac{G_3^2}{\Gamma_{30}} - \frac{G_1^2}{2\Gamma_{10} + G_2^2/\Gamma_{20} + \Gamma_{10}^2\Gamma_{20}/G_2^2} + \frac{G_1^2}{\Gamma_{10} + G_2^2/\Gamma_{20}} \right), \quad (9)$$

where A is the beam area, and the beam power P_2 is substituted by the corresponding Rabi frequency G_2 with relationship $G_i = (2\mu^2P_i/\hbar^2\varepsilon_0cA)^{1/2}$ taken into consideration. Note that $[G_1^2/(\Gamma_{10} + G_2^2/\Gamma_{20}) - G_1^2/(2\Gamma_{10} + G_2^2/\Gamma_{20} + \Gamma_{10}^2\Gamma_{20}/G_2^2)] > 0$, the result of this derivative is consistently a positive number. Thus, the detuning Δ_2 at resonant condition ($\Delta_2 + \Delta_1 + \varepsilon = 0$) will decrease when P_2 increases. This matches well with the experimental result in Fig. 3(a1). Therefore, the intensity of the Rydberg dressing field in the power-controlled Rydberg signal contributes not only to the signal intensity but also to the resonant position.

Subsequently, the influence of the temperature of the Rb atoms on the PA-SWM2 signals is investigated. The dependence of signal intensity on the temperature, which is proportional to the atomic density ρ , is clearly revealed by scanning Δ_2 in Fig. 3(b1). The saturation of the PA-SWM2 signal intensity can be observed in Fig. 3(b2). Particularly, along with the rise of the temperature, the growth rate of the PA-SWM2 signal intensity suffers a sharp decline. In order to interpret such an intensity saturation phenomenon, the atomic density should be considered together with the density-matrix element in Eq. (3) to describe the PA-SWM2 signal. Considering the Rydberg excitation, the PA-SWM2 signal intensity is proportional to $\rho_0^{0.2}\rho_{10}^{(5)}$ [38], in which ρ_0 is the density of the atoms. Therefore, the saturation caused by the rise of temperature can be attributed to the term $\rho_0^{0.2}$. Similarly, in the case of increasing the field power, the saturation of the signal intensity

can be attributed to term $(|G_2|/n^{11})^{0.2}$. However, owing to the relatively low power of E_2 in Fig. 3(a2), which is far from the saturation, the signal intensity keeps increasing with the increase of P_2 . One can find in Figs. 3(a2) and 3(b2) that when the parameters related to Rydberg excitation (such as the power and the atomic density) are of relatively low value, the suppression caused by RRI can be effectively eliminated. In the condition of low power and low temperature, the blockade domain in which only one excited Rydberg atom can exist is sufficiently large, considering Eq. (A4) in the Appendix A and $\rho_2V_d = 1$. Accordingly, Rydberg atoms can be so distant from each other that the RRI can be omitted. On the other hand, if the atomic population at the ground state increases, the probability for the Rydberg energy level to be occupied will be increased subsequently. However, the increase of the signal intensity will saturate because of the blockaded effect [40]. In addition, by enhancing the beam power, the number of Rydberg atoms will increase according to Eq. (A4), and the blockade radius will be reduced; hence, the distance between Rydberg atoms will be narrowed. Therefore, the RRI will be enhanced, and the average energy shift of the atoms will be larger. Consequently, the saturation of the PA-SWM2 signal intensity will occur if the beam power and the temperature increase continuously.

It can also be found that with the change of the temperature, the detuning Δ_2 for resonance also changes. Likewise, we can differentiate ε on the atomic density as

$$\frac{d\varepsilon}{d\rho} = 0.2C\rho_0^{-0.8} \left(\frac{|G_2|}{n^{11}} \right)^{0.4} \left(\frac{|G_1|^2}{\Gamma_{10} + G_2^2/\Gamma_{20}} + \frac{|G_3|^2}{\Gamma_{30}} \right)^{0.2}. \quad (10)$$

Obviously, the derivative in Eq. (10) is always positive, which illustrates that when the atomic density increases, ε will increase so that Δ_2 will decrease at the resonant condition ($\Delta_2 + \Delta_1 + \varepsilon = 0$). This result corresponds well with the experimental result shown in Fig. 3(b1). The corresponding theoretical simulation is shown in Fig. 3(b3). Therefore, the saturation of the signal intensity and the shift of resonant position of Rydberg signals can be achieved in the power-controlled and density-controlled PA-MWM process. It is also worth mentioning that the effect of parametric amplification can be affected by the temperature, since the Stokes field E_{St} and anti-Stokes field E_{ASt} of the OPA process depend on the atomic population [23]. Hence, the PA-SWM signal intensity increases more rapidly than the SWM signal does without parametric amplification, in comparison with our previous work [17].

In Fig. 4, we discuss the generation of EWM and the dependence of coexisting PA-SWM and PA-EWM on detuning and field intensity. When all the laser beams in the configuration in Fig. 1(b) are on, besides the aforementioned SWM1 and SWM2 signals, the EWM signal generated in the subsystem $|0\rangle \leftrightarrow |1\rangle \leftrightarrow |2\rangle \leftrightarrow |3\rangle \leftrightarrow |4\rangle$ is introduced into this system. The energy-level diagram with Autler–Townes (AT) splitting [41] is shown in Fig. 4(a1). Figure 4(a2) shows the schematic diagram in which the coexisting SWM and EWM signals are injected into the Stokes port to realize the OPA process. Along with PA-SWM2 signals, the Rydberg PA-EWM signals are also the constituent part of the detected PA-MWM signals, whose

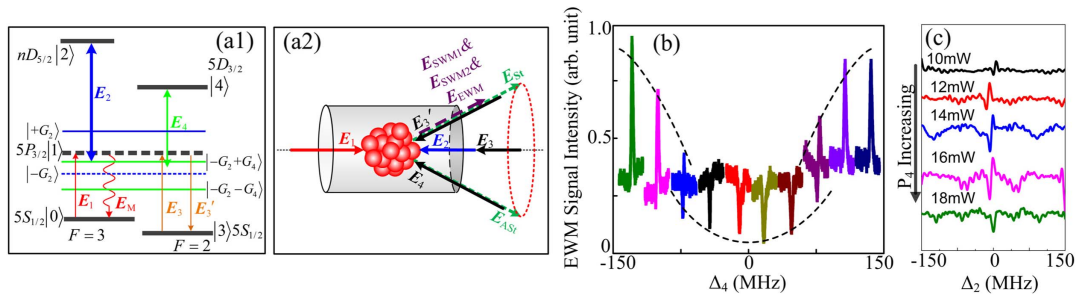


Fig. 4. (a1) AT splitting in the five-level atomic system induced by E_2 and E_4 ; (a2) phase-matching diagram of OPA injected with $E_{\text{SWM}1}$, $E_{\text{SWM}2}$, and E_{EWM} into the Stokes port. (b) Measured MWM versus Δ_2 with discrete Δ_4 for $n = 37$; the range of Δ_4 is from -150 to 150 MHz. (c) Measured MWM signals versus Δ_2 with increasing P_4 for $n = 37$; the range of P_4 is from 10 to 18 mW.

intensities are shown by scanning Δ_2 at several discrete values of Δ_4 in Fig. 4(b) and P_4 in Fig. 4(c). In Fig. 4(b), the Rydberg signals are detected with the background of a broadened FWM signal (generated in the Λ -type three-level subsystem $|0\rangle \leftrightarrow |1\rangle \leftrightarrow |3\rangle$) and a non-Rydberg SWM1 signal. The coexisting PA-EWM and PA-SWM signals obtained by scanning Δ_2 can be strengthened or suppressed at different values of Δ_4 [42]. Considering the dressing effects of both E_2 and E_4 , when the value of Δ_4 is far-detuned from the resonance of $|1\rangle \rightarrow |4\rangle$, coexisting SWM and EWM signals can only be enhanced, since the enhancement condition $\Delta_2 + \Delta_- + \Delta_{-+} = 0$ is the only extreme value condition that can be fulfilled. The additional detuning of primary and secondary dressing energy levels split by E_2 and E_4 is given by $\Delta_- = \{(\Delta_2 + \varepsilon) - [(\Delta_2 + \varepsilon)^2 + 4|G_2|^2]^{1/2}\}/2$ and $\Delta_{-+} = [\Delta_4' + (\Delta_4'^2 + 4|G_4|^2)]/2$, in which $\Delta_4' = \Delta_4 - \Delta_-$. It should be noted that the position of split energy level is also related to the term ε induced by RRI. These two split energy levels are denoted as $|-G_2\rangle$ and $|-G_2 + G_4\rangle$ in Fig. 4(a1). However, when the value of Δ_4 gradually approaches the resonance of $|1\rangle \leftrightarrow |4\rangle$, the influence of dressing field is gradually transformed from enhancement into suppression. In addition, when Δ_4 is near the resonant point, only the suppression of the output PA-MWM signal can be observed, because only the suppression condition $\Delta_2 + \Delta_1 = 0$ can be fulfilled. Meanwhile, it is possible for Δ_4 to be set to the value that both suppression and enhancement conditions can be satisfied; thus the half-enhancement and half-suppression of the output signal can be observed [42]. In this way, the signal can be enhanced or suppressed when the corresponding extreme value conditions ($\Delta_2 + \Delta_- + \Delta_{-+} = 0$ and $\Delta_2 + \Delta_1 = 0$) are satisfied. Similarly, as shown in the right part ($\Delta_4 > 0$) of Fig. 4(b), when Δ_4 continues to move far away from the resonance, the coexisting PA-SWM2 and PA-EWM signals will be enhanced by the dressing field again. The OPA process acts against the dressing suppression and enables the enhancement of the coexisting PA-SWM and PA-EWM signals to be more obvious. Furthermore, one can also notice that when we change the power of E_4 in Fig. 4(c), the effect of E_4 can also be switched between suppression and enhancement. When the power of the dressing field E_4 is relatively low, the signal is enhanced in Fig. 4(c). In this case, the suppression caused by the dressing effect of E_4 is not obvious, and both coexisting PA-SWM2 and PA-EWM signals

contribute to the peak in Fig. 4(c). Nevertheless, when P_4 increases gradually, the PA-MWM signals near the resonant position move gradually towards suppression with the transition of half-enhancement and half-suppression, as shown in Fig. 4(c). When the power P_4 is high enough, the suppression of the PA-MWM signals caused by the dressing effect of E_4 gets dominant, and dip is observed, as shown in the bottom of Fig. 4(c).

4. CONCLUSIONS

We have studied the PA-SWM and PA-EWM signals in a Rydberg EIT Rb atomic medium both experimentally and theoretically. The intensity dependences of the MWM signals on the principal quantum number, the detuning of the probe and coupling fields, the power of coupling fields, and the atomic density are investigated. One can find that the MWM signals can be effectively controlled by these parameters with the combined effect of RRI and the parametric amplification. Moreover, the linear amplification of the Rydberg MWM signals resulting from the OPA process acts against the suppression of the Rydberg excitation, which can potentially improve the logic gate devices and sensors related to Rydberg atoms.

APPENDIX A

SWM2 and EWM processes are related to the Rydberg transition. The mean-field model is applied to modify the density-matrix elements of $E_{\text{SWM}2}$ and E_{EWM} . It is considered that the region with only one excited Rydberg atom is a sphere with a radius of R_d , and the density of excited Rydberg atoms ρ_2 is supposed to be locally uniform inside and around the sphere; thus, we get $\rho_2 V_d = 1$, in which $V_d \propto R_d^3$ is the volume of the sphere. The level shift ε will be obtained as a function of its location r and the principal quantum number n as

$$\varepsilon = \rho_2 \int_{V'} U(r-r') d^3 r', \quad (\text{A1})$$

where $U(r-r')$ is the van der Waals interaction among Rydberg atoms, and it can be given as $\int_{V'} U(r-r') d^3 r' \propto 1/R_d^6$ for nD interaction. The optical Bloch equations for the Rydberg excitation ($5P_{3/2} \leftrightarrow nD_{5/2}$) are

$$i \frac{d}{dt} c_g = \frac{G_2}{2} e^{i\beta r^2} c_e, \quad (\text{A2})$$

$$i \frac{d}{dt} c_e = \varepsilon(r, t) c_e + \frac{G_2}{2} e^{-i\beta r^2} c_g, \quad (\text{A3})$$

where c_g and c_e are the probability amplitude for the ground state and Rydberg state, respectively.

Solving Eqs. (A1)–(A3) under steady-state approximation, then considering $\rho_2 V_d = 1$ and $V_d \propto R_d^3$, the density of the atoms excited to Rydberg state $|2\rangle$ can be given by [2,14]

$$\rho_2 = C \rho_1^{0.2} \left(\frac{|G_2|}{n^{11}} \right)^{0.4}, \quad (\text{A4})$$

where C is a constant related to numerical integration outside the given sphere and the atom excitation efficiency between $|0\rangle$ and $|1\rangle$, ρ_1 is the density of the atoms at $|1\rangle$, which is given by

$$\rho_1 = \frac{\rho_0}{2} \left[\frac{|G_1|^2}{\text{Re}(d_1 + |G_2|^2/d_2 + |G_4|^2/d_4)} + \frac{|G_3|^2}{\text{Re}(d_3)} \right], \quad (\text{A5})$$

where ρ_0 is the atomic density at the ground state $|0\rangle$, $d_1 = \Gamma_{10} + i\Delta_1$, $d_2 = \Gamma_{20} + i(\Delta_1 + \Delta_2)$, $d_3 = \Gamma_{30} + i(\Delta_1 - \Delta_3)$, and $d_4 = \Gamma_{30} + i(\Delta_1 + \Delta_4)$. Term $\rho_1^{0.2}$ indicates that the contribution of the particle number at $|1\rangle$ to the number of atoms excited to $|2\rangle$ is suppressed. Term $(|G_2|/n^{11})^{0.4}$ shows that the excitation caused by E_2 is also suppressed and limited by principal quantum number n . The dependence of ρ_2 on n in Eq. (A4) shows that the probability of atoms being excited to $|2\rangle$ will decrease with a larger n . Now that the energy shift ε in Eq. (A1) is directly related to the atomic density ρ_2 , ε is supposed to grow considerably larger with the increase of n or r within the given sphere, and accordingly, the Rydberg blockade effect is enhanced. Finally, we can substitute ρ_0 , G_1 , G_2 , and G_3 in the classical model with $\rho_0^{0.2}$, $G_1^{0.2}$, $(G_2/n^{11})^{0.2}$, and $G_3^{0.2}$, respectively, as a modification in the situation of Rydberg excitation.

Funding. National Key R&D Program of China (2017YFA0303700); National Natural Science Foundation of China (NSFC) (11474228, 11604256, 61605154); Key Scientific and Technological Innovation Team of Shaanxi Province (2014KCT-10); Natural Science Foundation of Shaanxi Province (2017JQ6039); China Postdoctoral Science Foundation (2016M600776).

[†]These authors contributed equally to this work.

REFERENCES

1. T. F. Gallagher, *Rydberg Atoms* (Cambridge University, 1994).
2. D. Tong, S. M. Farooqi, J. Stanojevic, S. Krishnan, Y. P. Zhang, R. Côté, E. E. Eyler, and P. L. Gould, "Local blockade of Rydberg excitation in an ultracold gas," *Phys. Rev. Lett.* **93**, 063001 (2004).
3. M. D. Lukin, M. Fleischhauer, R. Cote, L. M. Duan, D. Jaksch, J. I. Cirac, and P. Zoller, "Dipole blockade and quantum information processing in mesoscopic atomic ensembles," *Phys. Rev. Lett.* **87**, 037901 (2001).
4. M. Saffman, T. G. Walker, and K. Molmer, "Quantum information with Rydberg atoms," *Rev. Mod. Phys.* **82**, 2313–2363 (2010).
5. Y. O. Dudin and A. Kuzmich, "Strongly interacting Rydberg excitations of a cold atomic gas," *Science* **336**, 887–889 (2012).
6. G. Günter, M. Robert-De-Saint-Vincent, H. Schempp, C. S. Hofmann, S. Whitlock, and M. Weidemüller, "Interaction enhanced imaging of individual Rydberg atoms in dense gases," *Phys. Rev. Lett.* **108**, 013002 (2012).
7. N. Somaschi, V. Giesz, L. De Santis, J. C. Loredó, M. P. Almeida, G. Hornecker, S. L. Portalupi, T. Grange, C. Anton, J. Demory, C. Gomez, I. Sagnes, N. D. L. Kimura, A. Lemaitre, A. Auffeves, A. G. White, L. Lanco, and P. Senellart, "Near-optimal single-photon sources in the solid state," *Nat. Photonics* **10**, 340–345 (2016).
8. S. E. Harris, "Electromagnetically induced transparency," *Phys. Today* **50**, 36–42 (1997).
9. M. Xiao, Y. Li, S. Jin, and J. Geabanacloche, "Measurement of dispersive properties of electromagnetically induced transparency in rubidium atoms," *Phys. Rev. Lett.* **74**, 666–669 (1995).
10. A. J. Merriam, S. J. Sharpe, M. Shverdin, D. Manuszak, G. Y. Yin, and S. E. Harris, "Efficient nonlinear frequency conversion in an all-resonant double- Λ system," *Phys. Rev. Lett.* **84**, 5308–5311 (2000).
11. Z. Zhang, H. Tang, I. Ahmed, N. Ahmed, G. Khan, A. Mahesar, and Y. Zhang, "Controlling Rydberg-dressed four-wave mixing via dual electromagnetically induced transparency windows," *J. Opt. Soc. Am. B* **33**, 1661–1667 (2016).
12. C. Carr, M. Tanasittikosol, A. Sargsyan, D. Sarkisyan, C. S. Adams, and K. J. Weatherill, "Three-photon electromagnetically induced transparency using Rydberg states," *Opt. Lett.* **37**, 3858–3860 (2012).
13. E. Brekke, J. O. Day, and T. G. Walker, "Four-wave mixing in ultracold atoms using intermediate Rydberg states," *Phys. Rev. A* **78**, 063830 (2008).
14. Z. Zhang, J. Che, D. Zhang, Z. Liu, X. Wang, and Y. Zhang, "Eight-wave mixing process in a Rydberg-dressing atomic ensemble," *Opt. Express* **23**, 13814–13822 (2015).
15. Y. Zhang, U. Khadka, B. Anderson, and M. Xiao, "Temporal and spatial interference between four-wave mixing and six-wave mixing channels," *Phys. Rev. Lett.* **102**, 013601 (2009).
16. A. Kölle, G. Eppe, H. Kübler, R. Löw, and T. Pfau, "Four-wave mixing involving Rydberg states in thermal vapor," *Phys. Rev. A* **85**, 063821 (2012).
17. H. B. Zheng, X. Yao, Z. Y. Zhang, J. L. Che, Y. Q. Zhang, Y. P. Zhang, and M. Xiao, "Blocked six- and eight-wave mixing processes tailored by electromagnetically induced transparency scissors," *Laser Phys.* **24**, 045404 (2014).
18. M. D. Lukin, A. B. Matsko, M. Fleischhauer, and M. O. Scully, "Quantum noise and correlations in resonantly enhanced wave mixing based on atomic coherence," *Phys. Rev. Lett.* **82**, 1847–1850 (1999).
19. T. Peyronel, O. Firstenberg, Q. Y. Liang, S. Hofferberth, A. V. Gorshkov, T. Pohl, M. D. Lukin, and V. Vuletić, "Quantum nonlinear optics with single photons enabled by strongly interacting atoms," *Nature* **488**, 57–60 (2012).
20. V. Boyer, A. M. Marino, R. C. Pooser, and P. D. Lett, "Entangled images from four-wave mixing," *Science* **321**, 544–547 (2008).
21. Z. Bai and G. Huang, "Enhanced third-order and fifth-order Kerr nonlinearities in a cold atomic system via Rydberg-Rydberg interaction," *Opt. Express* **24**, 4442–4461 (2016).
22. Z. Zhang, H. Zheng, X. Yao, Y. Tian, J. Che, X. Wang, D. Zhu, Y. Zhang, and M. Xiao, "Phase modulation in Rydberg dressed multi-wave mixing processes," *Sci. Rep.* **5**, 10462 (2015).
23. Z. Zhang, F. Wen, J. Che, D. Zhang, C. Li, Y. Zhang, and M. Xiao, "Dressed gain from the parametrically amplified four-wave mixing process in an atomic vapor," *Sci. Rep.* **5**, 15058 (2015).
24. Y. Zhang, M. Belić, Z. Wu, H. Zheng, K. Lu, Y. Li, and Y. Zhang, "Soliton pair generation in the interactions of Airy and nonlinear accelerating beams," *Opt. Lett.* **38**, 4585–4588 (2013).
25. M. A. Foster, A. C. Turner, J. E. Sharping, B. S. Schmidt, M. Lipson, and A. L. Gaeta, "Broad-band optical parametric gain on a silicon photonic chip," *Nature* **441**, 960–963 (2006).
26. J. K. Thompson, J. Simon, H. Loh, and V. Vuletić, "A high-brightness source of narrowband, identical-photon pairs," *Science* **313**, 74–77 (2006).
27. Y. P. Zhang, A. W. Brown, and M. Xiao, "Opening four-wave mixing and six-wave mixing channels via dual electromagnetically induced transparency windows," *Phys. Rev. Lett.* **99**, 123603 (2007).
28. M. H. Rubin, D. N. Klyshko, Y. H. Shih, and A. V. Sergienko, "Theory of two-photon entanglement in type-II optical parametric down-conversion," *Phys. Rev. A* **50**, 5122–5133 (1994).

29. J. M. Wen and M. H. Rubin, "Transverse effects in paired-photon generation via an electromagnetically induced transparency medium. II. Beyond perturbation theory," *Phys. Rev. A* **74**, 023809 (2006).
30. C. F. McCormick, A. M. Marino, V. Boyer, and P. D. Lett, "Strong low-frequency quantum correlations from a four-wave-mixing amplifier," *Phys. Rev. A* **78**, 043816 (2008).
31. R. C. Pooser and B. Lawrie, "Plasmonic trace sensing below the photon shot noise limit," *ACS Photon.* **3**, 8–13 (2015).
32. R. C. Pooser and B. Lawrie, "Ultrasensitive measurement of micro-cantilever displacement below the shot-noise limit," *Optica* **2**, 393–399 (2015).
33. F. Hudelist, J. Kong, C. Liu, J. Jing, Z. Y. Ou, and W. Zhang, "Quantum metrology with parametric amplifier-based photon correlation interferometers," *Nat. Commun.* **5**, 3049 (2014).
34. J. A. Sedlacek, A. Schwettmann, H. Kübler, R. Löw, T. Pfau, and J. P. Shaffer, "Microwave electrometry with Rydberg atoms in a vapour cell using bright atomic resonances," *Nat. Phys.* **8**, 819–824 (2012).
35. P. P. Herrmann, J. Hoffnagle, N. Schlumpf, V. L. Telegdi, and A. Weis, "Stark spectroscopy of forbidden two-photon transitions: a sensitive probe for the quantitative measurement of small electric fields," *J. Phys. B* **19**, 1271–1280 (1986).
36. S. Mukamel, *Principles of Nonlinear Optical Spectroscopy* (Oxford University, 1995).
37. H. Zheng, X. Zhang, Z. Zhang, Y. Tian, H. Chen, C. Li, and Y. Zhang, "Parametric amplification and cascaded-nonlinearity processes in common atomic system," *Sci. Rep.* **3**, 1885 (2013).
38. H. Chen, Y. Zhang, X. Yao, Z. Wu, X. Zhang, Y. Zhang, and M. Xiao, "Parametrically amplified bright-state polariton of four- and six-wave mixing in an optical ring cavity," *Sci. Rep.* **4**, 3619 (2014).
39. Y. Li, G. Huang, D. Zhang, Z. Wu, Y. Zhang, J. Che, and Y. Zhang, "Density control of dressed four-wave mixing and super-fluorescence," *IEEE J. Quantum Electron.* **50**, 25–34 (2014).
40. J. Che, J. Ma, H. Zheng, Z. Zhang, X. Yao, Y. Zhang, and Y. Zhang, "Rydberg six-wave mixing process," *Europhys. Lett.* **109**, 33001 (2015).
41. Y. P. Zhang, P. Y. Li, H. B. Zheng, Z. G. Wang, H. X. Chen, C. B. Li, R. Zhang, and Y. Zhang, "Observation of Autler-Townes splitting in six-wave mixing," *Opt. Express* **19**, 7769–7777 (2011).
42. P. Li, H. Zheng, Y. Zhang, J. Sun, C. Li, G. Huang, Z. Zhang, Y. Li, and Y. Zhang, "Controlling the transition of bright and dark states via scanning dressing field," *Opt. Mater.* **35**, 1062–1070 (2013).